PERGAMON

International Journal of Heat and Mass Transfer 42 (1999) 1123–1140

International Journal of
HEAT and MASS
TRANSFER

Solution of inverse heat conduction problems using control volume approach

J. Taler*, W. Zima

Cracow University of Technology, Institute of Process and Power Engineering, ul. Warszawska 24, 31-155 Kraków, Poland

Received 17 March 1997; in final form 31 July 1997

Abstract

A new method for solving multidimensional inverse heat conduction problems is presented. Using control volume methods, the partial heat conduction equation is replaced by a system of ordinary differential equations in time, which are then solved sequentially. The procedure is started at a spatial node where temperature sensor is located and sequentially marches through space to the surface node. The accuracy of the method was demonstrated by comparison of the calculated surface heat flux and temperature with the known exact solution. Two numerical experiments, one- and two-dimensional inverse heat conduction problems, are solved to illustrate the effectiveness, computational efficiency and good accuracy of the presented method. In the third example, the inverse formulation is applied to a set of experimental data. The method can easily be extended to three-dimensional cases. © 1998 Elsevier Science Ltd. All rights reserved.

Nomenclature

a	width of the plate [m]
b	length of the plate [m]
$Bi_1 = h_1 \cdot b/k$, $Bi_2 = h_2 \cdot a/k$	Biot numbers
c	heat capacity [J kg^{-1} K^{-1}]
E	sensor depth below heated surface [m]
f	smoothed measured value of temperature at time t [°C]
$\bar{f}$	measured value of temperature at time t [°C]
$f_3 = f$	smoothed measured value of temperature at third spatial node [°C]
$Fo = \alpha \cdot t/L^2$	Fourier number for one-dimensional problems
$Fo_1 = \alpha \cdot t/b^2$, $Fo_2 = \alpha \cdot t/a^2$	Fourier numbers for two-dimensional problems
$h(t)$	heat transfer coefficient [W m^{-2} K^{-1}]
k	thermal conductivity [W m^{-1} K^{-1}]
L	thickness of the plate [m]
N	total number of data points
NT	number of measurement points in moving average filter
q	heat flux [W m^{-2}]
q_c	estimated heat flux for errorless data [W m^{-2}]
$q_{c,p}$	estimated heat flux for data with errors [W m^{-2}]
q_E	heat flux at the sensor location [W m^{-2}]
q_N	nominal heat flux of the triangular test case [W m^{-2}]
q_2	surface heat flux [W m^{-2}]
r	radius [m]
r_{in}	inner radius of cylinder [m]
r_{out}	outer radius of cylinder [m]
s	measured value of temperature after spatial smoothing [°C]
t	time [s]
T	temperature [°C]
T_0	initial temperature [°C]
T_s	surface temperature [°C]
$T_\infty(t)$	fluid temperature [°C]
x, y	Cartesian coordinates.

Greek symbols

α	thermal diffusivity [m^2 s^{-1}]
β_i, γ_i	roots of characteristic equations
ΔFo	dimensionless time step
Δt	time step [s]
Δx, Δy	spatial sizes of control volumes [m]
Θ	dimensionless temperature
λ	random variable of normal distribution with zero mean

---

* Corresponding author

PII: S0017-9310(98)00280-4

ρ density [kg m^{-3}]
σ standard deviation of the measurement errors.

Subscripts and superscripts
c calculated
ex exact
E measurement location
f measurement temperature
i spatial node index
j temporal node index
p approximated
q heat flux
s surface
t total
$+$ dimensionless
∞ ambient.

1. Introduction

The inverse heat conduction problem (IHCP) is defined as the estimation of the boundary conditions from transient temperature measurements at one or more interior locations. Due to the ill-posedness of the IHCP, it is more difficult to solve than the direct problem. In the past two decades various solution methods have been developed to handle the one-dimensional IHCP [1–5]. However, very few studies have been published on the multi-dimensional IHCP [6–12]. One-dimensional IHCP are very often solved using the space marching methods [13–16]. In these techniques stabilizing future measurement times are inherently used. A major disadvantage of the space marching finite difference methods is stiff coupling of time and space grid points. The number of future time steps depends on the number of spatial grid points, not on the physics of the problem. Furthermore, the space marching procedures utilize exact matching of the calculated temperature with the measured temperature and thus are sensitive to measurement errors. Despite the relatively large interest expressed in multi-dimensional IHCP, most of the reported studies have presented techniques which require considerable amounts of computational power to solve the IHCP.

In this paper, the control volume approach in conjunction with the method of lines is employed to solve the IHCP when the temperature field depends on more than one spatial coordinate. The proposed method is simple and capable of handling two- and three-dimensional problems. Its accuracy is comparable with other techniques, while the programming effort and computation time can be substantially less.

The presented technique produces accurate and reliable results without iteration and step by step computation in the time domain until the specific time reached. Past and future time data are incorporated within the algorithm, but the number of these steps is independent of the number of spatial node points.

2. Analysis

In this section we pose the problem of inverse heat conduction in one and two dimensions. Using the control volume approach, the partial differential equation is replaced by a system of ordinary differential equations. The time derivatives are not approximated by finite differences (the method of lines).

2.1. One-dimensional IHCP

First, consider the one-dimensional linear inverse heat conduction problem in cylindrical coordinate system illustrated in Fig. 1a. The flux and temperature are assumed to be known as discrete functions of time at the location $r = r_{\mathrm{E}}$:

$$T(r_{\mathrm{E}}, t) = f(t) \tag{1}$$

$$q_{\mathrm{E}} = -k\left.\frac{\partial T}{\partial r}\right|_{r=r_{\mathrm{E}}}. \tag{2}$$

The heat flux (2) at $r = r_{\mathrm{E}}$ can be found from the solution for the temperature distribution in $r_{\mathrm{E}} \leqslant r \leqslant r_{\mathrm{out}}$, since the problem in this space domain can be analyzed as the direct heat conduction problem. Thus, two conditions are specified at $r = r_{\mathrm{E}}$ and none at $r = r_{\mathrm{in}}$. The thermophysical properties of the solid are assumed to be independent of temperature. The boundary condition at $r = r_{\mathrm{out}}$ is known. The ambient temperature T_∞ is known from measurements. It is desired to predict the heat flux and the temperature history at the exposed surface $r = r_{\mathrm{in}}$.

The heat transfer coefficient is given by:

$$h(t) = \frac{q_{\mathrm{s}}(t)}{T_\infty - T(r_{\mathrm{in}}, t)} \tag{3}$$

where:

$$q_{\mathrm{s}}(t) = -k\left.\frac{\partial T(r, t)}{\partial r}\right|_{r=r_{\mathrm{in}}}. \tag{4}$$

In order to solve the IHCP the inverse domain $r_{\mathrm{in}} \leqslant r \leqslant r_{\mathrm{E}}$ is divided into the three control volumes. Due to the location of the known conditions, it is reasonable to begin with a heat balance for node 3 located at $r = r_{\mathrm{E}}$:

$$\pi(r_4^2 - r_3^2)c\rho\frac{\mathrm{d}f_3}{\mathrm{d}t} = \frac{2\pi r_3 k}{\Delta r}(T_2 - f_3) + \frac{2\pi r_4 k}{\Delta r}(T_4 - f_3). \tag{5}$$

Similar equations are derived for two other nodes, 2 and 1:

$$\pi(r_3^2 - r_2^2)c\rho\frac{\mathrm{d}T_2}{\mathrm{d}t} = \frac{2\pi r_2 k}{\Delta r}(T_1 - T_2) + \frac{2\pi r_3 k}{\Delta r}(T_3 - T_2) \tag{6}$$

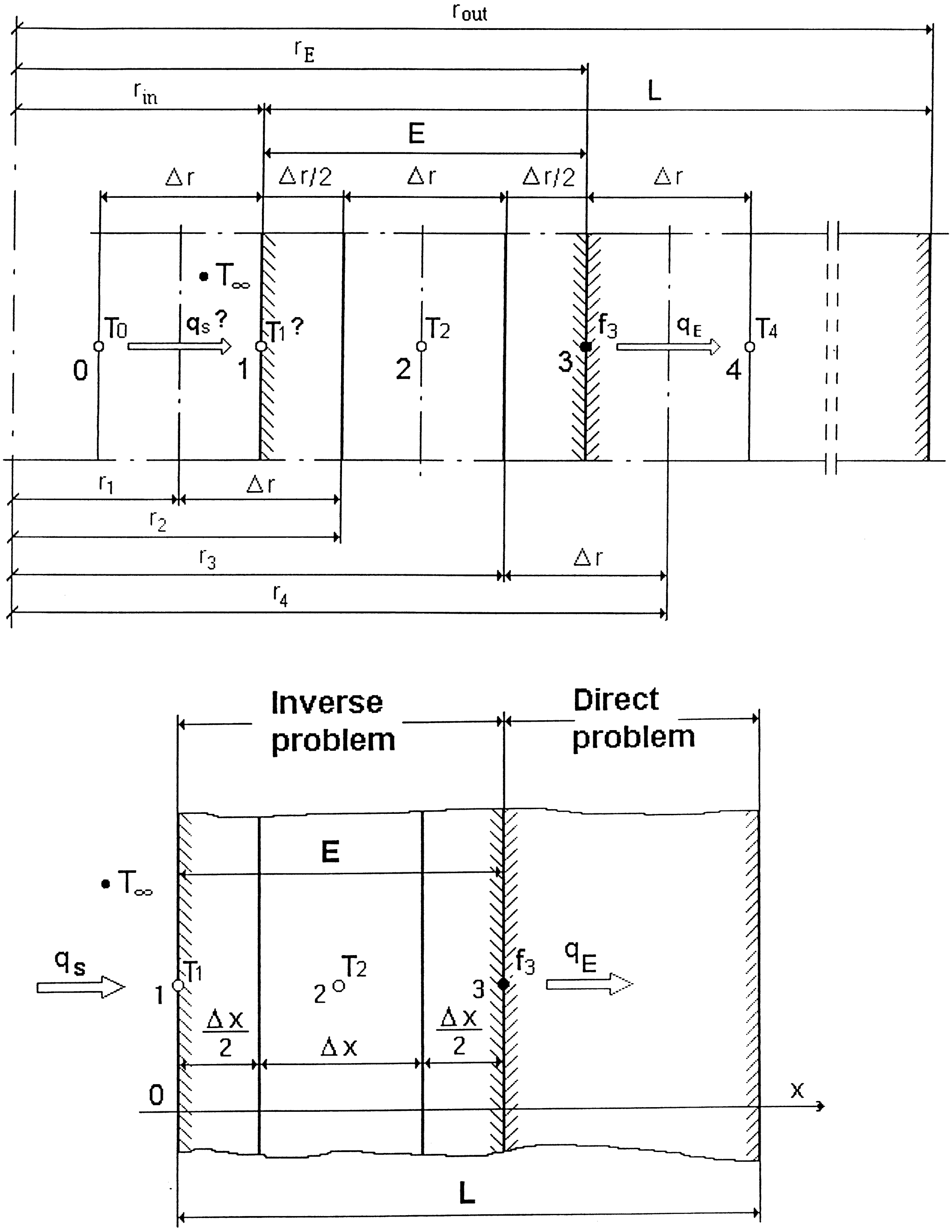

Fig. 1. One-dimensional inverse heat conduction problem with control volume grid in inverse domain.

$$\pi(r_2^2-r_1^2)c\rho\frac{\mathrm{d}T_1}{\mathrm{d}t}=\frac{2\pi r_1 k}{\Delta r}(T_0-T_1)+\frac{2\pi r_2 k}{\Delta r}(T_2-T_1) \tag{7}$$

where $\Delta r=(r_\mathrm{E}-r_\mathrm{in})/2$.

The temperatures T_4 and T_0 at fictious nodes outside the inverse domain are calculated from the following central difference approximation for boundary conditions at $r=r_\mathrm{E}$ and $r=r_\mathrm{in}$ (Fig. 1):

$$-k\frac{T_4-T_2}{2\Delta r}=q_\mathrm{E} \tag{8}$$

and

$$-k\frac{T_2-T_0}{2\Delta r}=q_\mathrm{s}. \tag{9}$$

Solving these equations for the temperatures T_4 and T_0 yields:

$$T_4=T_2-\frac{2q_\mathrm{E}\Delta r}{k} \tag{10}$$

and

$$T_0=T_2+\frac{2q_\mathrm{s}\Delta r}{k}. \tag{11}$$

Substituting equation (10) into equation (5) and solving it for the temperature T_2 yields:

$$T_2=f_3+\frac{1}{2}\frac{(\Delta r)^2}{\alpha}\frac{\mathrm{d}f_3}{\mathrm{d}t}+\frac{r_4}{r_3+r_4}\frac{2q_\mathrm{E}\Delta r}{k} \tag{12}$$

where $\alpha=k/c\rho$.

As the calculation proceeds from the right-hand boundary to the left, the temperature T_1 will be established as equation (12) is substituted into the heat balance equation (6):

$$T_1=f_3+\frac{r_2+r_3}{r_2}\left[\frac{(\Delta r)^2}{\alpha}\frac{\mathrm{d}f_3}{\mathrm{d}t}+\frac{(\Delta r)^4}{4\alpha^2}\frac{\mathrm{d}^2f_3}{\mathrm{d}t^2}\right.$$
$$\left.+\frac{2r_4}{r_3+r_4}\frac{q_\mathrm{E}\Delta r}{k}+\frac{r_4}{r_3+r_4}\frac{(\Delta r)^3}{\alpha k}\frac{\mathrm{d}q_\mathrm{E}}{\mathrm{d}t}\right]. \tag{13}$$

The surface heat flux is calculated from the heat balance equation (7) at the surface node:

$$q_\mathrm{s}(t)=(r_2+r_3)\left[\frac{k\Delta r}{2\alpha}\left(\frac{1}{r_1}+\frac{1}{r_2}\right)\frac{\mathrm{d}f_3}{\mathrm{d}t}\right.$$
$$+\frac{k(\Delta r)^3}{4\alpha^2}\left(\frac{r_1+r_2}{r_1r_2}+\frac{1}{2r_1}+\frac{1}{2r_2}\right)\frac{\mathrm{d}^2f_3}{\mathrm{d}t^2}$$
$$\left.+\frac{k(\Delta r)^5}{16\alpha^3}\frac{r_1+r_2}{r_1r_2}\frac{\mathrm{d}^3f_3}{\mathrm{d}t^3}\right]$$
$$+q_\mathrm{E}\frac{r_4}{r_3+r_4}\left(\frac{r_3-r_1}{r_1}+\frac{r_2+r_3}{r_2}\right)$$
$$+\frac{(r_2+r_3)r_4}{r_3+r_4}\left[\frac{(\Delta r)^2}{2\alpha}\left(\frac{r_1+r_2}{r_1r_2}+\frac{1}{r_1}+\frac{1}{r_2}\right)\frac{\mathrm{d}q_\mathrm{E}}{\mathrm{d}t}\right.$$
$$\left.+\frac{(\Delta r)^4}{4\alpha^2}\frac{r_1+r_2}{r_1r_2}\frac{\mathrm{d}^2q_\mathrm{E}}{\mathrm{d}t^2}\right]. \tag{14}$$

When $r_1, r_2, r_3, r_4\to\infty$, the equations (13) and (14) are reduced to the following expressions:

$$T_1=T_\mathrm{s}=f_3+\frac{1}{2}\frac{E^2}{\alpha}\frac{\mathrm{d}f_3}{\mathrm{d}t}+\frac{1}{32}\frac{E^4}{\alpha^2}\frac{\mathrm{d}^2f_3}{\mathrm{d}t^2}$$
$$+\frac{q_\mathrm{E}E}{k}+\frac{1}{8}\frac{E^3}{k\alpha}\frac{\mathrm{d}q_\mathrm{E}}{\mathrm{d}t} \tag{15}$$

and

$$q_\mathrm{s}=q_\mathrm{E}+k\left[\frac{E}{\alpha}\frac{\mathrm{d}f_3}{\mathrm{d}t}+\frac{3}{16}\frac{E^3}{\alpha^2}\frac{\mathrm{d}^2f_3}{\mathrm{d}t^2}\right.$$
$$\left.+\frac{1}{128}\frac{E^5}{\alpha^3}\frac{\mathrm{d}^3f_3}{\mathrm{d}t^3}\right]+\frac{1}{2}\frac{E^2}{\alpha}\frac{\mathrm{d}q_\mathrm{E}}{\mathrm{d}t}$$
$$+\frac{1}{32}\frac{E^4}{\alpha^2}\frac{\mathrm{d}^2q_\mathrm{E}}{\mathrm{d}t^2} \tag{16}$$

where $E=2\Delta x$, Δx-control volume thickness (Fig. 2) and f_3 is smoothed measured temperature at the third node.

The above equations are the approximate solution of the inverse heat conduction problem for planar geometry (Fig. 1).

Equations (15) and (16) are the numerical analogues of the exact solution given by Stefan [19] and Burggraf [20]. Truncating the infinite series in the exact solution after two terms gives:

$$T_1=T_\mathrm{s}=f_3+\frac{1}{2}\frac{E^2}{\alpha}\frac{\mathrm{d}f_3}{\mathrm{d}t}+\frac{1}{24}\frac{E^4}{\alpha^2}\frac{\mathrm{d}^2f_3}{\mathrm{d}t^2}+\frac{q_\mathrm{E}E}{k}$$
$$+\frac{1}{6}\frac{E^3}{k\alpha}\frac{\mathrm{d}q_\mathrm{E}}{\mathrm{d}t}+\frac{1}{120}\frac{E^5}{k\alpha^2}\frac{\mathrm{d}^2q_\mathrm{E}}{\mathrm{d}t^2} \tag{17}$$

$$q_\mathrm{s}=q_\mathrm{E}+k\left[\frac{E}{\alpha}\frac{\mathrm{d}f_3}{\mathrm{d}t}+\frac{1}{6}\frac{E^3}{\alpha^2}\frac{\mathrm{d}^2f_3}{\mathrm{d}t^2}\right]+\frac{1}{2}\frac{E^2}{\alpha}\frac{\mathrm{d}q_\mathrm{E}}{\mathrm{d}t}$$
$$+\frac{1}{24}\frac{E^4}{\alpha^2}\frac{\mathrm{d}^2q_\mathrm{E}}{\mathrm{d}t^2}. \tag{18}$$

An examination of the formulas (15) and (17) indicates that the first difference between the finite control volume method and exact solutions are different coefficients on the time derivatives. Additional difference is the lack of the second-order time derivative of the heat flux q_E in equation (15). In the case of the heat flux [equations (16) and (18)] the third derivative of the measured temperature $f_3(t)$ appears only in the developed solution (16). This is very advantageous because in all inverse problems it is much more difficult to determine the surface heat flux than the surface temperature. The third derivative term in equation (16) allows to determine q_s with higher accuracy.

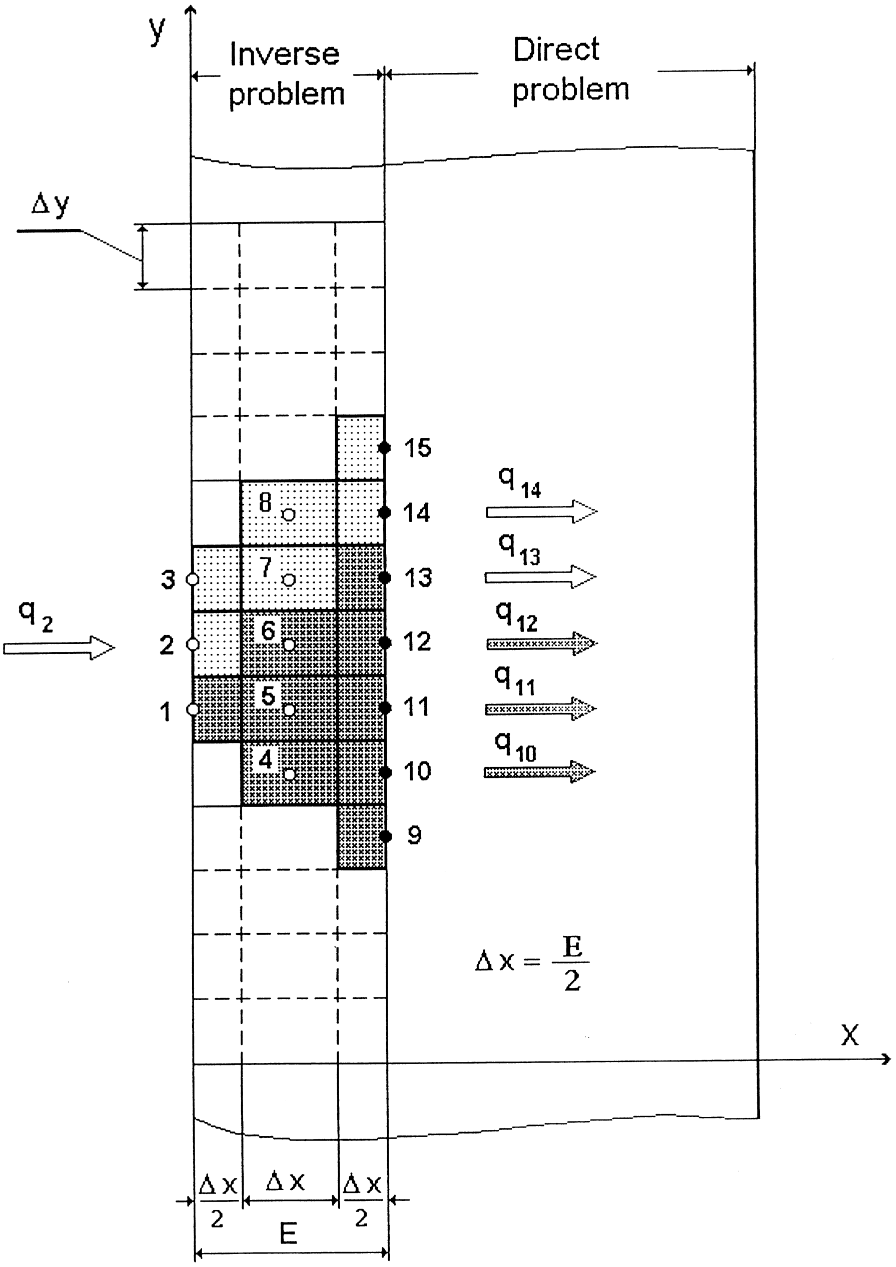

Fig. 2. Two-dimensional inverse heat conduction problem.

As the number of control volumes increases, higher derivatives appear in the approximate solutions (15) and (16). To calculate correctly the surface heat flux and temperature time derivative of the measured temperature $f(t)$ and the related heat flux $q_E(t)$ should be evaluated with high accuracy. The finite difference interpolation is the predominant numerical technique for determination of function derivatives, but because of its low accuracy is inappropriate in this case. Interpolation is effective as a means of constructing derivative approximations only if sufficiently accurate data values are available. Otherwise, other methods of approximation must be used.

The problem of the order of time derivatives in the inverse solution is very complex. When the input data are exact and infinite differentiable then accounting for the high-order times derivatives in the inverse solution improves its accuracy. On the other hand, it is well known that differentiation of noisy data is basically an unstable process. If the data being differentiated are from experimental tests, or are observations subject to errors of measurement, the errors so influence the higher-order derivative values calculated by finite differences that they may be meaningless. The usual recommendation is to smooth the data first. The numerical experiments carried out with exact and our space marching methods have shown that its no use accounting for time derivatives higher than the third- of fourth-order.

In this paper, the time derivatives $\mathrm{d}^n f/\mathrm{d}t^n$ and $\mathrm{d}^n q_{\mathrm{E}}/\mathrm{d}t^n$, $n = 0, 1, 2, \ldots$, are calculated using local least squares approximation of temperature and heat flux data with low-order polynomials. For a smoother approximation of transient temperature history and its derivatives one has to go to piecewise polynomial approximation. The digital filter approach is use, because it can be demonstrated that it is much more computationally efficient than global approximation methods. Due to its efficiency, it can be readily implemented in an on-line method of analysis. The time derivatives are determined from local approximation of the data points using Gram polynomial [21]. The local approximation means that the coefficients of a third-order polynomial depend only on a small number of equally spaced data points. Extensive numerical experiments have shown that for optimal results seven, nine or eleven data points should be taken. The smoothed values of functions representing temperature history and its derivatives are calculated only at the centre point. Given the data $\tilde{f}(t), \tilde{f}(t+\Delta t), \ldots, \tilde{f}[t+(NT-1)\Delta t]$, first we construct the third-order Gram polynomial and then calculate its value and derivatives at the centre point: $t+(NT-1)\Delta t/2$. In similar fashion, the smoothed value of $q_{\mathrm{E}}(t)$ and its derivatives are calculated. As stated, the order of the highest time derivative of the measured temperature $f(t)$ in the inverse solution for $q_s(t)$ is equal to the number of control volumes into which the inverse region is subdivided. Accounting for the higher order-time derivatives $f^n(t)$ in the inverse solution results in its better accuracy if the temperature $f(t)$ at $x = E$ (Fig. 1) is exact. However, this feature of the method does not lend itself readily to practical calculation using actual data. The quality of the reconstruction of the boundary condition depends first of all on the distance E between sensor and the active surface. For example, if point $x = E$ is located so far that it does not indicate any changes in the boundary condition at $x = 0$ during the given time interval, it is impossible to find the solution of the inverse problem. If the changes of boundary condition cause measurable temperature changes, then the inverse problem can be solved properly. The estimated boundary condition is averaged over the time step used in the inverse analysis. When the temperature sensor is located deep under the active surface or at the rear surface, then the high-frequency components of the input signal at the active surface are attenuated inside the body and not indicated by the temperature sensor at $x = E$. The measured temperature changes at $x = E$ are also delayed in comparison to the boundary condition changes. Then, it is very difficult or impossible to determine the high-frequency components of the input signal and the initial condition by using the high-order time derivatives in the inverse solution based on temperature measurements far from the active surface. The only effective way to determine fast time changes of the temperature or heat flux at the active surface is to place the temperatures sensor near this surface. In order to reconstruct the boundary condition with high accuracy based on the temperature measurements at the interior location $x = E$, it is sufficient to divide the inverse region $0 \leqslant x \leqslant E$ into three or four control volumes. The developed method can easily be applied for solving inverse problems in composite bodies.

2.2. *Two-dimensional IHCP*

A simple domain (Fig. 2) is considered to study the use of the developed method in solving the transient two-dimensional IHCP. The problem consists in determining the temperature and heat flux at node 2 at the exposed surface from the known temperature $\tilde{f}(E, y)$ at $x = E$. To calculate the surface heat flux at node 2, the temperature at adjacent nodes 1 and 3 must also be determined. Consider a two-dimensional grid as shown in Fig 2 with $\Delta x \neq \Delta y$. There are seven embedded thermocouples 9–15, all with a coordinate of $x = E$.

The heat balance equations are first written for nodes 10, 11 and 12, at which temperature is already known from measurement:

$$c\rho\frac{\Delta x}{2}\Delta y\frac{\mathrm{d}f_{10}}{\mathrm{d}t} = k\frac{f_9-f_{10}}{\Delta y}\frac{\Delta x}{2}+k\frac{T_4-f_{10}}{\Delta x}\Delta y + k\frac{f_{11}-f_{10}}{\Delta y}\frac{\Delta x}{2}-q_{10}\Delta y \quad (19)$$

$$c\rho\frac{\Delta x}{2}\Delta y\frac{\mathrm{d}f_{11}}{\mathrm{d}t} = k\frac{f_{10}-f_{11}}{\Delta y}\frac{\Delta x}{2}+k\frac{T_5-f_{11}}{\Delta x}\Delta y + k\frac{f_{12}-f_{11}}{\Delta y}\frac{\Delta x}{2}-q_{11}\Delta y \quad (20)$$

$$c\rho\frac{\Delta x}{2}\Delta y\frac{\mathrm{d}f_{12}}{\mathrm{d}t} = k\frac{f_{11}-f_{12}}{\Delta y}\frac{\Delta x}{2}+k\frac{T_6-f_{12}}{\Delta x}\Delta y + k\frac{f_{13}-f_{12}}{\Delta y}\frac{\Delta x}{2}-q_{12}\Delta y. \quad (21)$$

Solving equations (19)–(21) for the temperature at nodes 4, 5 and 6, respectively, one obtains:

$$T_4 = f_{10}+\frac{(\Delta x)^2}{2\alpha}\frac{\mathrm{d}f_{10}}{\mathrm{d}t}-\frac{(\Delta x)^2}{2(\Delta y)^2}(f_9-2f_{10}+f_{11})+q_{10}\frac{\Delta x}{k} \quad (22)$$

$$T_5 = f_{11} + \frac{(\Delta x)^2}{2\alpha}\frac{\mathrm{d}f_{11}}{\mathrm{d}t} - \frac{(\Delta x)^2}{2(\Delta y)^2}(f_{10} - 2f_{11} + f_{12}) + q_{11}\frac{\Delta x}{k} \quad (23)$$

$$T_6 = f_{12} + \frac{(\Delta x)^2}{2\alpha}\frac{\mathrm{d}f_{12}}{\mathrm{d}t} - \frac{(\Delta x)^2}{2(\Delta y)^2}(f_{11} - 2f_{12} + f_{13}) + q_{12}\frac{\Delta x}{k}. \quad (24)$$

A heat balance equation for node 5 is:

$$c\rho\Delta x\Delta y\frac{\mathrm{d}T_5}{\mathrm{d}t} = k\frac{T_4 - T_5}{\Delta y}\Delta x + k\frac{T_1 - T_5}{\Delta x}\Delta y + k\frac{T_6 - T_5}{\Delta y}\Delta x + k\frac{f_{11} - T_5}{\Delta x}\Delta y \quad (25)$$

which when solved for T_1 yields:

$$T_1 = 2T_5 + \frac{(\Delta x)^2}{\alpha}\frac{\mathrm{d}T_5}{\mathrm{d}t} - \frac{(\Delta x)^2}{(\Delta y)^2}(T_4 - 2T_5 + T_6) - f_{11}. \quad (26)$$

Substituting T_4, T_5 and T_6 given by expressions (22)–(24), respectively, into equation (26) and rearranging gives:

$$\begin{aligned} T_1 = {} & f_{11} + \frac{2(\Delta x)^2}{\alpha}\frac{\mathrm{d}f_{11}}{\mathrm{d}t} + \frac{(\Delta x)^4}{2\alpha^2}\frac{\mathrm{d}^2 f_{11}}{\mathrm{d}t^2} \\ & - \frac{2(\Delta x)^2}{(\Delta y)^2}(f_{10} - 2f_{11} + f_{12}) \\ & + \frac{(\Delta x)^4}{(\Delta y)^4}\left(\frac{1}{2}f_9 - 2f_{10} + 3f_{11} - 2f_{12} + \frac{1}{2}f_{13}\right) \\ & + 2q_{11}\frac{\Delta x}{k} + \frac{(\Delta x)^3}{\alpha k}\frac{\mathrm{d}q_{11}}{\mathrm{d}t} \\ & - \frac{(\Delta x)^3}{(\Delta y)^2 k}(q_{10} - 2q_{11} + q_{12}) \\ & - \frac{(\Delta x)^4}{\alpha(\Delta y)^2}\left(\frac{\mathrm{d}f_{10}}{\mathrm{d}t} - 2\frac{\mathrm{d}f_{11}}{\mathrm{d}t} + \frac{\mathrm{d}f_{12}}{\mathrm{d}t}\right). \end{aligned} \quad (27)$$

Using equation (27) the temperature at nodes located at $x = 0$ can be determined in similar fashion. Having calculated the temperature at nodes 1, 3 and 6, the surface heat flux at node 2 can be obtained. Using a heat balance on node 2, which is undergoing heat transfer with the environment, one obtains:

$$c\rho\frac{\Delta x}{2}\Delta y\frac{\mathrm{d}T_2}{\mathrm{d}t} = k\frac{T_1 - T_2}{\Delta y}\frac{\Delta x}{2} + k\frac{T_3 - T_2}{\Delta y}\frac{\Delta x}{2} + k\frac{T_6 - T_2}{\Delta x}\Delta y + q_2\Delta y. \quad (28)$$

The solution to this equation is:

$$q_2 = k\left[\frac{\Delta x}{2\alpha}\frac{\mathrm{d}T_2}{\mathrm{d}t} - \frac{\Delta x}{2(\Delta y)^2}(T_1 - 2T_2 + T_3) - \frac{T_6 - T_2}{\Delta x}\right]. \quad (29)$$

If the grid array is square ($\Delta x = \Delta y$), the expression for T_1 becomes:

$$\begin{aligned} T_1 = {} & 8f_{11} - 4f_{10} - 4f_{12} + \frac{1}{2}f_9 \\ & + \frac{1}{2}f_{13} + \frac{E^2}{\alpha}\frac{\mathrm{d}f_{11}}{\mathrm{d}t} + \frac{E^4}{32\alpha^2}\frac{\mathrm{d}^2 f_{11}}{\mathrm{d}t^2} \\ & - \frac{E^2}{4\alpha}\frac{\mathrm{d}f_{10}}{\mathrm{d}t} - \frac{E^2}{4\alpha}\frac{\mathrm{d}f_{12}}{\mathrm{d}t} + \frac{2E}{k}q_{11} \\ & + \frac{E^3}{8\alpha k}\frac{\mathrm{d}q_{11}}{\mathrm{d}t} - \frac{E}{2k}q_{10} - \frac{E}{2k}q_{12}. \end{aligned} \quad (30)$$

Examining the equations (27) and (29) reveals that the temperature and heat flux at surface node 2 are affected only by a few number of measured quantities at $x = E$. Only changes in temperature and heat flux in very close domain to the analysed node have an influence on the estimated temperature and heat flux at this node.

An inverse domain can be divided into nonregular or nonrectangular grids. If the body is irregularly shaped, then the developed method can also be used. In such a case instead of applying the classical control volume method, the control volume finite-element method should be used [21, 22].

3. Smoothing of temperature data

The solutions (15) and (16), as well as (27) and (29), show the dependence of the surface temperature and heat flux on high-orders of time derivatives of the measured temperature and the related heat flux both at $x = E$. The IHCP is ill-posed. Therefore, the solutions are very sensitive to measurement errors in input data. Variations in the surface conditions of the body are attenuated at interior locations of the body. Conversely the small measurement errors in the data are magnified at the surface and may cause large oscillations in the estimated surface temperature and heat flux. To minimize the effects of noisy data the measured temperature and heat flux at $x = E$ should be smoothed before they are used in the IHCP algorithm. Least squares approximation is very well suited for the recovery of a smooth function from noisy information. It is possible to chose an appropriate function which is flexible enough to reconstruct the underlying noisefree function and its derivatives while still orthogonal to the noise, i.e., unable to follow the oscillations in the measured data. Because of the low accuracy of derivative approximations by finite-differences they will not be considered in this paper. The Gram orthogonal polynomial [23] are used for smoothing of measured time-temperature history. Assuming that measurement points $\bar{f}(y_i, t_j)$ are equally spaced in time and in the y-direction, we construct a piecewise cubic polynomial and then use a least squares procedure to estimate appropriate polynomial coefficients. Piecewise polynomials have lately become more widely used in least squares data fitting since they are more flexible than simple polynomials. Most of the methods assume that the beginning and the end of the data are fixed. However, for on-line systems, it is frequently necessary to follow and fit the data without knowing its end beforehand. In case of the local method the approximating Gram polynomial depends only on a few of the nearest data points. A set of neighbouring data points is not large; usually 7, 9 or 11 data points are used. The value of smoothing Gram polynomial and its derivatives will be calculated only at the centre of the approximation interval, while for determining of polynomial coefficients future and past data points, usually 3, 4 or 5, are used. Using the estimated Gram polynomial a moving averaging filter is constructed [18]. The smoothed value of time-space-temperature history is calculated by filtering in two independent directions, y and t. To fit a surface $f(y, t)$ through data on rectangular grid $(y_i, t_j, \bar{f}_{i,j})$ the two-way univariate approximation is used. First, the filtering is applied to measured data, keeping t_j fixed and varying i, and then by applying it again to the resulting sets of spatially smoothed data points, but this time keeping y_i fixed and varying j. The first smoothing gives a least squares fit to the seven data points $\bar{f}_{i,j}$, $i-3$, $i-2, \ldots, i, \ldots, i+2$, $i+3$ for $t_j = \text{const}$ (Fig. 3). The smoothed values of temperature $s_{i,j}$ at spatial nodes 9–15 are obtained using moving seven-point digital filters, which results from the aforementioned least-squares approximation by Gram polynomial:

$$s_{i-3,j} = \tfrac{1}{42}(39\bar{f}_{i-3,j} + 8\bar{f}_{i-2,j} - 4\bar{f}_{i-1,j} - 4\bar{f}_{i,j} + \bar{f}_{i+1,j} + 4\bar{f}_{i+2,j} - 2\bar{f}_{i+3,j}) \quad (31)$$

$$s_{i-2,j} = \tfrac{1}{42}(8\bar{f}_{i-3,j} + 19\bar{f}_{i-2,j} + 16\bar{f}_{i-1,j} + 6\bar{f}_{i,j} - 4\bar{f}_{i+1,j} - 7\bar{f}_{i+2,j} + 4\bar{f}_{i+3,j}) \quad (32)$$

$$s_{i-1,j} = \tfrac{1}{42}(-4\bar{f}_{i-3,j} + 16\bar{f}_{i-2,j} + 19\bar{f}_{i-1,j} + 12\bar{f}_{i,j} + 2\bar{f}_{i+1,j} - 4\bar{f}_{i+2,j} + \bar{f}_{i+3,j}) \quad (33)$$

$$s_{i,j} = \tfrac{1}{21}(-2\bar{f}_{i-3,j} + 3\bar{f}_{i-2,j} + 6\bar{f}_{i-1,j} + 7\bar{f}_{i,j} + 6\bar{f}_{i+1,j} + 3\bar{f}_{i+2,j} - 2\bar{f}_{i+3,j}) \quad (34)$$

$$s_{i+1,j} = \tfrac{1}{42}(\bar{f}_{i-3,j} - 4\bar{f}_{i-2,j} + 2\bar{f}_{i-1,j} + 12\bar{f}_{i,j} + 19\bar{f}_{i+1,j} + 16\bar{f}_{i+2,j} - 4\bar{f}_{i+3,j}) \quad (35)$$

$$s_{i+2,j} = \tfrac{1}{42}(4\bar{f}_{i-3,j} - 7\bar{f}_{i-2,j} - 4\bar{f}_{i-1,j} + 6\bar{f}_{i,j} + 16\bar{f}_{i+1,j} + 19\bar{f}_{i+2,j} + 8\bar{f}_{i+3,j}) \quad (36)$$

$$s_{i+3,j} = \tfrac{1}{42}(-2\bar{f}_{i-3,j} + 4\bar{f}_{i-2,j} + \bar{f}_{i-1,j} - 4\bar{f}_{i,j} - 4\bar{f}_{i+1,j} + 8\bar{f}_{i+2,j} + 39\bar{f}_{i+3,j}). \quad (37)$$

The spatially fitted data points are smoothed once again using eleven point time averaging digital filter (Fig. 4):

$$f(y_i, t_j) = \frac{1}{429}(-36s_{i,j-5} + 9s_{i,j-4} + 44s_{i,j-3} + 69s_{i,j-2} + 84s_{i,j-1} + 89s_{i,j} + 84s_{i,j+1} + 69s_{i,j+2} + 44s_{i,j+3} + 9s_{i,j+4} - 36s_{i,j+5}) \quad (38)$$

$$f'(y_i, t_j) = \frac{1}{5148\Delta t}(300s_{i,j-5} - 294s_{i,j-4} - 532s_{i,j-3} - 503s_{i,j-2} - 296s_{i,j-1} + 296s_{i,j+1} + 503s_{i,j+2} + 532s_{i,j+3} + 294s_{i,j+4} - 300s_{i,j+5}) \quad (39)$$

$$f''(y_i, t_j) = \frac{5}{143(\Delta t)^2}\left(s_{i,j-5} + \frac{2}{5}s_{i,j-4} - \frac{1}{15}s_{i,j-3} - \frac{2}{5}s_{i,j-2} - \frac{3}{5}s_{i,j-1} - \frac{2}{3}s_{i,j} - \frac{3}{5}s_{i,j+1} - \frac{2}{5}s_{i,j+2} - \frac{1}{15}s_{i,j+3} + \frac{2}{5}s_{i,j+4} + s_{i,j+5}\right) \quad (40)$$

$$f'''(y_i, t_j) = \frac{5}{143(\Delta t)^3}\left(-s_{i,j-5} + \frac{1}{5}s_{i,j-4}\right.$$

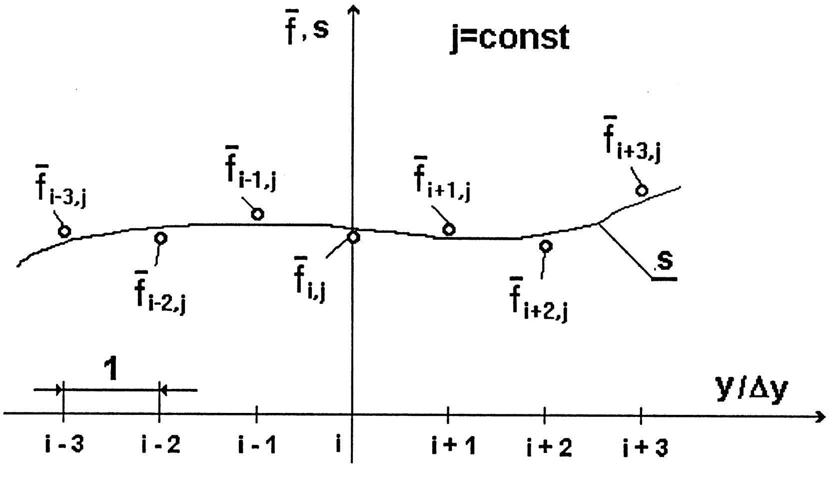

Fig. 3. Spatial smoothing of the measured temperatures using seven point averaging filter.

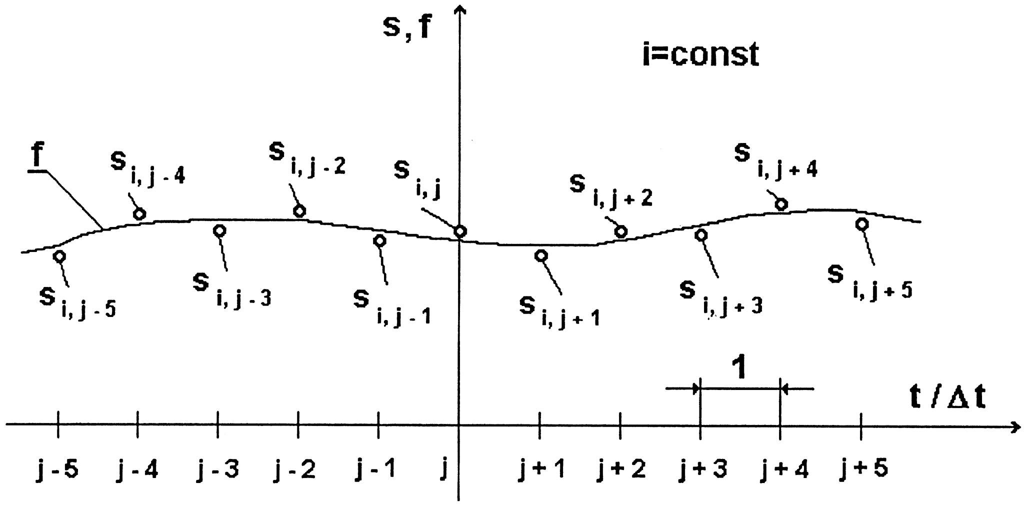

Fig. 4. Time smoothing of the measured temperatures using eleven point averaging filter.

$$+\frac{11}{15}s_{i,j-3}+\frac{23}{30}s_{i,j-2}+\frac{7}{15}s_{i,j-1}-\frac{7}{15}s_{i,j+1}$$
$$\left.-\frac{23}{30}s_{i,j+2}-\frac{11}{15}s_{i,j+3}-\frac{1}{5}s_{i,j+4}+s_{i,j+5}\right). \tag{41}$$

The temperature history and its time derivatives are evaluated at the centre point j. In equations we consider future and past data, where the $j+1,\ldots,j+5$ are the future data and those $j-1,\ldots,j-5$ are the past data. Having calculated the temperature and its derivatives at the center point, the whole time interval $10\Delta t$ is moved one time step forward dropping the last data point ($j-5$) and adding a new one. Since no past data is available in the first interval, the calculations should start at least five steps before heating or cooling starts. If this is done, the equations (38)–(41) can be used for $t_j = 0$, i.e. when the real process begins. In one-dimensional IHCP there is no need to spatially smooth the data. In this case one can assume $s_{i,j} = \bar{f}_{i,j}$ in equations (38)–(41). On the other hand, in two-dimensional steady-state IHCP, the time smoothing is dropped.

4. Algorithm testing

In order to test the accuracy of the developed method the two numerical examples are presented. Although all experiments have error, studying the effects of errorless measurements can give insight into the maximum possible resolution of surface conditions available from the measurements. The only error introduced into the problem is the error due to computer roundoff. To illustrate the power of the method, it was implemented on an IBM PC 486 using single precision arithmetic. Therefore, the exact and 'noisy' data will be considered.

4.1. One-dimensional IHCP test case

One of the standard test cases for comparing results of inverse heat conduction algorithms is for a triangular heat flux. The geometry is a flat plate and the sensor is located at the surface: $x = E = L$, which is insulated. This test case is thoroughly discussed by Beck et al., Chap 5 [1]. The heat flux is zero before time zero and is again zero after dimensionless time 1.2, with a triangular flux in between and a maximum occurring at time $Fo = 0.6$ (Figs 5 and 6). The simulated temperature measurements with errors added have been taken from [1]. The noisy

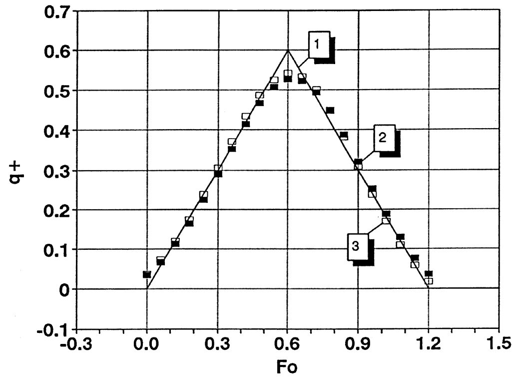

Fig. 5. Calculated surface heat flux for triangular heat flux; errorless data, 1, applied surface heat flux, 2, estimated heat flux using Stefan–Burggraf–Langford method, 3, present method.

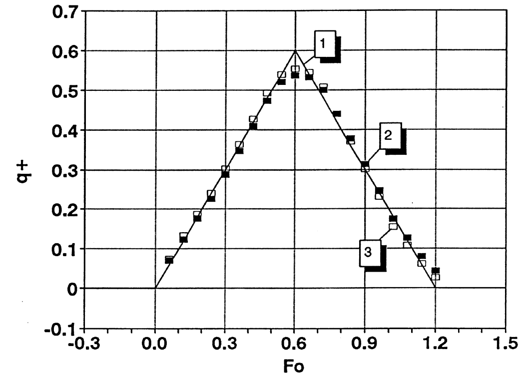

Fig. 6. Calculated surface heat flux for triangular heat flux; data with random errors, 1, applied surface heat flux, 2, estimated heat flux using Stefan–Burggraf–Langford method, 3, present method.

data $\bar{f}(t)$ is obtained by adding a random error to T_j, i.e., $\bar{f}_j = T_j + \varepsilon_j$, where T_j is exact temperature and ε_j is a Gausian random variable of variance σ^2.

The square root of the variance is given by:

$$\sigma_f^+ = \frac{k}{q_N L}\sqrt{\frac{1}{N}\sum_{j=1}^{N}(T_j|_{x=L} - \bar{f}_j)^2}. \tag{42}$$

The dimensionless time steps are $\Delta Fo = 0.06$. For this example, the following parameter values are used: $T_0 = 20°\mathrm{C}$, $L = 0.1$ m, $k = 52$ W m^{-1} K^{-1}, $\alpha = 14.4 \cdot 10^{-6}\,\mathrm{m^2\,s^{-1}}$, $\Delta t = 41.7$ s ($\Delta Fo = 0.06$), $q_N = 10^5$ W m^{-2}.

The results for the test case with errorless data are shown in Fig. 5. For errors equal to $\sigma_f^+ = 0.0017$ (about 0.5% of the maximum temperature rise of the measured temperature) the results shown in Fig. 6 are nearly as good as for no measurement errors. The exact and noisy temperature data $\bar{f}_j$ were smoothed using eleven point averaging filter. The exact solution of the IHCP [19, 20] for the same data produced results that are surprisingly close to those of the presented method. The series in the exact solution were truncated after the second term. If the discretized computed heat flux component is denoted $q_{c,p}^+(t_j)$ and the true (exact) component is $q_{ex}^+(t_j)$, in order to measure the error, the sample root mean square norm is introduced; it is given by:

$$\sigma_{q,t}^+ = \sqrt{\frac{1}{N}\sum_{j=1}^{N}[q_{ex}^+(t_j) - q_{c,p}^+(t_j)]^2}. \tag{43}$$

The sensitivity of the method to random errors is given by:

$$\sigma_q^+ = \sqrt{\frac{1}{N}\sum_{j=1}^{N}[q_c^+(t_j)|_{\sigma_f^+=0} - q_{c,p}^+(t_j)]^2}. \tag{44}$$

The root mean squared errors in q for $\sigma_f^+ = 0.0017$ are:

$\sigma_{q,t}^+ = 0.01714$ and $\sigma_q^+ = 0.00888$ for the presented method and $\sigma_{q,t}^+ = 0.02132$ and $\sigma_q^+ = 0.008047$ for the exact method.

The $\sigma_{q,t}^+/\sigma_f^+$ and σ_q^+/σ_f^+ ratios for both methods are given below:

- $(\sigma_{q,t}^+/\sigma_f^+) = 10.1$ and $(\sigma_q^+/\sigma_f^+) = 5.2$ for the presented method,
- $(\sigma_{q,t}^+/\sigma_f^+) = 12.5$ and $(\sigma_q^+/\sigma_f^+) = 4.7$ for the exact method.

The same problem was solved for three different divisions of the inverse region into control volumes (Fig. 7). The temperature data $\bar{f}(t)$ are approximated by the Gram polynomial of the 4th degree, because the fourth-order time derivatives of $f(t)$ are included in the inverse solution for $q_s(t)$, when division shown in Fig. 7c is used. The smoothed values of the function $f(t)$ are calculated in the middle of the time interval including eleven data pairs: $(t_i, \bar{f}_i)$, $i = 1, \ldots, 11$. Smoothing the data locally, the time derivatives are calculated using central difference formulas [24]:

$$f'_j = \frac{-\bar{f}_{j+2} + 8\bar{f}_{j+1} - 8\bar{f}_{j-1} - \bar{f}_{j-2}}{12\Delta t}$$

$$f''_j = \frac{-\bar{f}_{j+2} + 16\bar{f}_{j+1} - 30\bar{f}_j + 16\bar{f}_{j-1} - \bar{f}_{j-2}}{12(\Delta t)^2}$$

$$f'''_j = \frac{\bar{f}_{j+2} - 2\bar{f}_{j+1} + 2\bar{f}_{j-1} - \bar{f}_{j-2}}{2(\Delta t)^3}$$

$$f''''_j = \frac{\bar{f}_{j+2} - 4\bar{f}_{j+1} + 6\bar{f}_j - \bar{f}_{j-1} + \bar{f}_{j-2}}{(\Delta t)^4}. \tag{45}$$

Results for two, three and four control volumes for triangular heat flux case with errorless data are displayed in Fig. 8. In the case of two control volumes the results are not satisfactory. The agreement with the exact input heat flux is very good for three and four control volumes. If four control volumes are used, the results are a little better than for three control volumes. Similar results are shown in Fig. 5 for three control volumes with temperature data smoothed by the Gram polynomial of the 3rd degree. It can be concluded that increasing the number of control volumes over three does not bring noticeable improvement into the result accuracy.

In addition, the effect of the random errors is much larger (see Fig. 9), when the temperature data are approximated by the polynomial of the fourth order. Larger errors in this case, when compared with Fig. 6, are partially caused by unprecise calculation of the time derivatives using simple formulas (45).

The $\sigma_{q,t}^+/\sigma_f^+$ and σ_q^+/σ_f^+ ratios for different number of control volumes are given below:

- $(\sigma_{q,t}^+/\sigma_f^+) = 47.4$ and $(\sigma_q^+/\sigma_f^+) = 19.5$ for two control volumes,

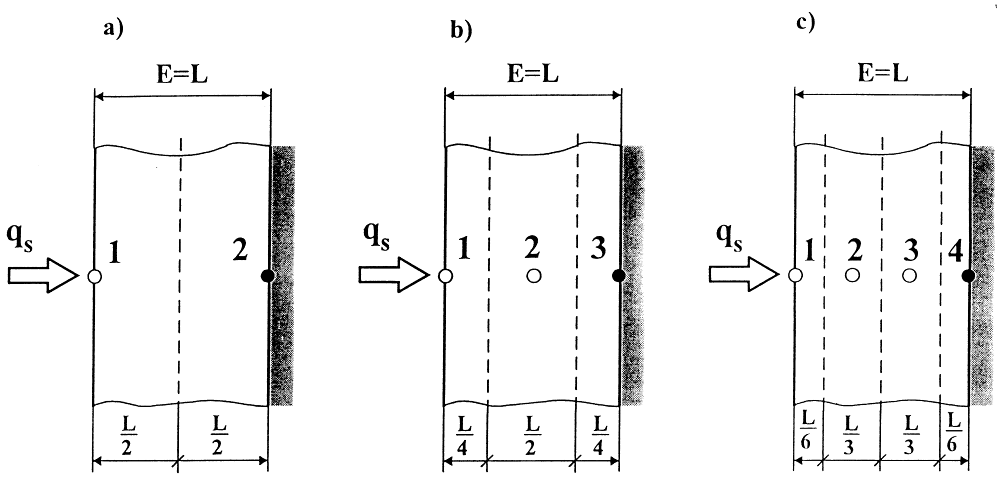

Fig. 7. Control volume grid for a plate; (a) two, (b) three, (c) four control volumes, respectively.

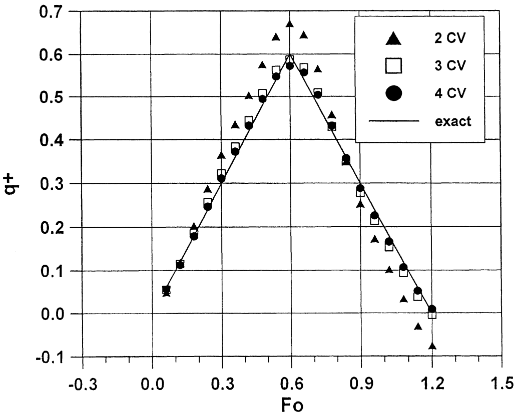

Fig. 8. Calculated surface heat flux for triangular heat flux case with errorless data for various number of control volumes (CV).

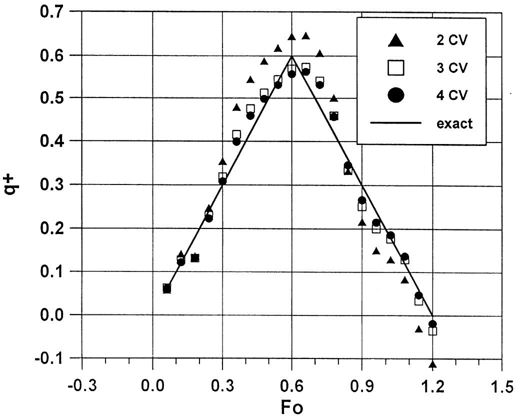

Fig. 9. Calculated surface heat flux for triangular heat flux case with perturbated data for various number of control volumes (CV).

- $(\sigma^+_{q,\mathrm{t}}/\sigma^+_{\mathrm{f}}) = 20.5$ and $(\sigma^+_q/\sigma^+_{\mathrm{f}}) = 14.6$ for three control volumes,
- $(\sigma^+_{q,\mathrm{t}}/\sigma^+_{\mathrm{f}}) = 16.4$ and $(\sigma^+_q/\sigma^+_{\mathrm{f}}) = 12.6$ for four control volumes.

To assess the accuracy of the time derivative calculated numerically, dimensionless standard deviations for f', f'', and f''' were calculated according to:

$$\sigma f^{+(n)} \cong \left\{\frac{1}{N}\sum_{i=1}^{N}\left[\left(\frac{\partial^n T^+(1,Fo)}{\partial Fo^n}\right)_{\mathrm{ex}} - \frac{\partial^n f^+}{\partial Fo^n}\right]^2\right\}^{1/2} \tag{46}$$

where n is the order of the time derivative, $T^+(1,Fo)$ is the dimensionless exact and f^+ is the dimensionless 'measured' temperature at an insulated surface, respectively.

A dimensionless derivative of the nth-order is defined by:

$$\frac{\partial^n T^+}{\partial Fo^n} = \frac{kL^{2n-1}}{\alpha^n}\frac{1}{q_{\mathrm{N}}}\frac{\partial^n T}{\partial t^n}. \tag{47}$$

The exact derivatives $\partial^n T^+/\partial Fo^n$ were calculated analytically. It can be seen, from the Table 1 that the fourth-

Table 1
Dimensionless standard deviations for time derivates of 'measured' temperature

Order of the derivative	1	2	3
Polynomial of the third-order			
Exact data	0.00502899	0.1692607	2.010108
Data with errors	0.00777597	0.1588959	2.204246
Polynomial of the fourth-order			
Exact data	0.00524026	0.0700228	2.026719
Data with errors	0.00722447	0.1598057	2.161686

order Gram polynomial and the finite difference formulas (45) do not give any improvement in the results if the data are perturbed. Much better is the polynomial of the third-order that ensures high accuracy of the calculated derivatives both for errorless and perturbated data.

It is worth noting that the results obtained by using the four control volumes are only slightly better than those for the three control volumes, if the temperature data are exact (Figs 5 and 8). The division of the inverse region into three control volumes in conjunction with data filtering based on the Gram polynomial of the 3rd degree can be recommended for the solution of the inverse heat conduction problems in one dimension.

It can be concluded that the presented method is computationally efficient, accurate and not too sensitive to measurement errors.

4.2. Two-dimensional IHCP test case

In order to examine the accuracy of the method as applied to the analysis of the two-dimensional IHCP, we consider a rectangular bar of width b and height a. The simulated temperature data are generated by solving the direct heat condition problem. The bar is at a uniform initial temperature T_0 and is exposed to a convective environment on the top and right surfaces, and insulated on the remaining two sides (Fig. 10). The following are the characteristics of this test case:

$a = 0.02\,\mathrm{m}$, $b = 0.07\,\mathrm{m}$, $k = 50\,\mathrm{W\,m^{-1}\,K^{-1}}$,

$c = 480\,\mathrm{J\,kg^{-1}\,K^{-1}}$, $\rho = 7.85\cdot 10^3\,\mathrm{kg\,m^{-3}}$, $T_0 = 20°\mathrm{C}$

$T_\infty = 100°\mathrm{C}$, $h_1 = 1071.43\,\mathrm{W\,m^{-2}\,K^{-1}}(Bi_1 = 1.5)$

and $h_2 = 500\,\mathrm{W\,m^{-2}\,K^{-1}}(Bi_2 = 0.2)$.

In order to artificially generate the temperature data at nodes (9)–(15) (Fig. 10), the direct problem was solved using analytical technique:

$$T(x,y,t) = \Theta(x,y,t)(T_0 - T_\infty) + T_\infty \tag{48}$$

$$\Theta(x,y,t) = \Theta_x(x,t)\cdot\Theta_y(y,t) = \sum_{i=1}^{\infty}\frac{2\sin\beta_i\cos(\beta_i x/b)\exp(-\beta_i^2 Fo_1)}{\beta_i + \sin\beta_i\cos\beta_i}\cdot\sum_{i=1}^{\infty}\frac{2\sin\gamma_i\cos(\gamma_i y/a)\exp(-\gamma_i^2 Fo_2)}{\gamma_i + \sin\gamma_i\cos\gamma_i} \tag{49}$$

where:

$$Fo_1 = \frac{\alpha t}{b^2}, \quad Fo_2 = \frac{\alpha t}{a^2}.$$

The nondimensional temperature $\Theta_x(x,t)$ is the solution for one-dimensional transient conduction in the x-direction across a width b. The temperature $\Theta_y(y,t)$ is the solution in the y-direction across a height a. The Biot and Fourier numbers for each of the one-dimensional solutions are based upon the characteristic lengths b and a, respectively. The eigenvalues β_i and γ_i are the roots of the following transcendental equations:

$$\frac{\beta\sin\beta}{\cos\beta} - Bi_1 = 0 \tag{50}$$

and

$$\frac{\gamma\sin\gamma}{\cos\gamma} - Bi_2 = 0 \tag{51}$$

where:

$$Bi_1 = \frac{h_1 b}{k}, \quad Bi_2 = \frac{h_2 a}{k}.$$

The first twelve eigenvalues of equations (50) and (51) are displayed in Table 2. The temperatures calculated from equation (48) were considered exact measurements, T_{ex}, and the simulated measured temperature data, $\bar{f}$, containing small measurement errors, were determined as:

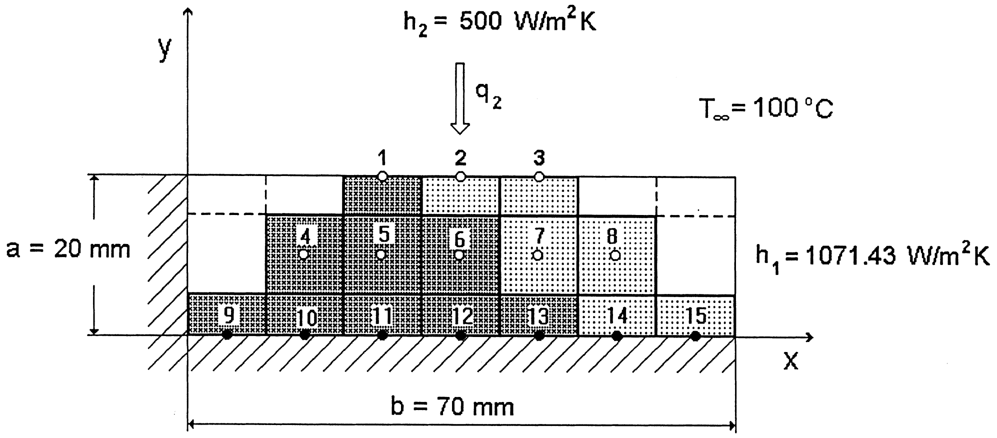

Fig. 10. Estimating of surface heat flux and heat transfer coefficient at node 2 using temperature measurements at nodes 9–15.

Table 2
Roots of transcendental equations (50) and (51)

i	β_i	γ_i
1	0.98824	0.43284
2	3.54217	3.20394
3	6.50966	6.31484
4	9.58009	9.44595
5	12.68408	12.58226
6	15.80260	15.72069
7	18.92863	18.86016
8	22.05904	22.00024
9	25.19221	25.14069
10	28.32724	28.28140
11	31.46356	31.42229
12	34.60085	34.56330

$$\tilde{f} = T_{\mathrm{ex}} + \lambda\sigma \tag{52}$$

were $\lambda\sigma$ is the error term and σ is the selected standard deviation for the measured data. For normally distributed errors, with zero mean and 99.7% confidence bound, λ lies within the range: $-3 \leqslant \lambda \leqslant 3$. The random variable λ is calculated by the IBM subroutine [25]. For all test cases analyzed here, we considered $\sigma = 0$ (errorless measurements) and $\sigma = 0.05$ (inexact measurements) with $\Delta t = 3$ s. Figure 11 shows exact temperature measurements of nodes (9)–(15). Figures 12 and 13 illustrate the numerical experiment results for the exact temperature data and Figs 14 and 15 for the noisy data. The agreement between estimated and exact temperatures at nodes 1–3 is excellent, for both situations of errorless and noisy measurements (Figs 12 and 14). The estimated heat flux and heat transfer coefficient are compared with the known true values in Figs 13 and 15. The estimated values match the data very well. The numerical experiments were performed using time and space smoothing both for the exact and noisy data.

Instead of relying on visual comparisons, we again give the root mean squared errors in h:

$$\sigma_{\mathrm{h,t}} = \sqrt{\frac{1}{N}\sum_{j=1}^{N}[h_{\mathrm{ex}}(t_j) - h_{\mathrm{c,p}}(t_j)]^2} \tag{53}$$

$$\sigma_{\mathrm{h}} = \sqrt{\frac{1}{N}\sum_{j=1}^{N}[h_{\mathrm{c,ex}}(t_j) - h_{\mathrm{c,p}}(t_j)]^2}. \tag{54}$$

The errors $\sigma_{\mathrm{h,t}}$ and σ_{h} are 65.9 W m^{-2} K^{-1} and 10.8 W m^{-2} and K^{-1}, respectively. In order to determine temperatures at nodes adjacent to the exposed surface, the heat balance equations for nodes close to the sides $x = 0$ and $x = b$ should be written.

4.3. Example utilizing actual measured data

In the third example, the inverse formulation is applied to a set of experimental data. A tube having an inside radius of $r_{\mathrm{in}} = 0.1085$ m and an outside radius of $r_{\mathrm{out}} = 0.1385$ m, made of 13CrMo44 (Grade 31) steel was heated on the inside surface by a fluid of the known temperature T_∞. The tube is perfectly insulated at the external surface. In this experiment, the cylinder whose wall temperature is at first uniform was heated suddenly

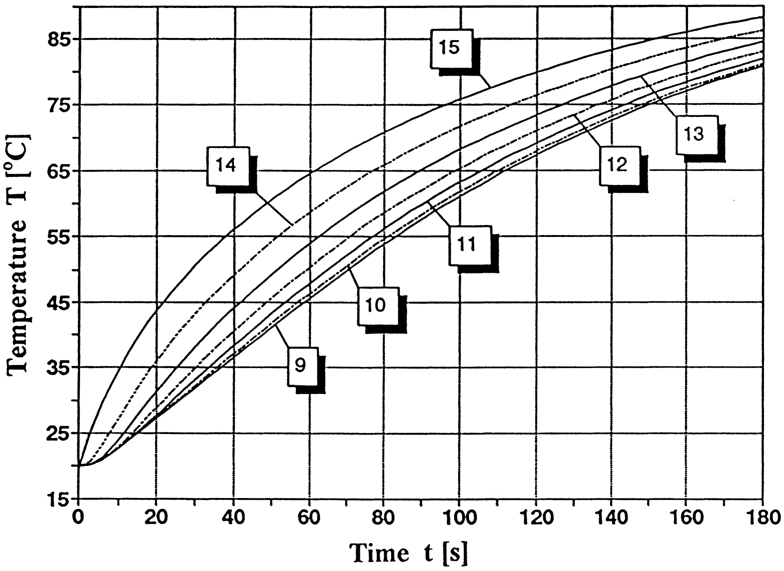

Fig. 11. Discrete temperature data from the direct solution use to simulate exact temperature measurements.

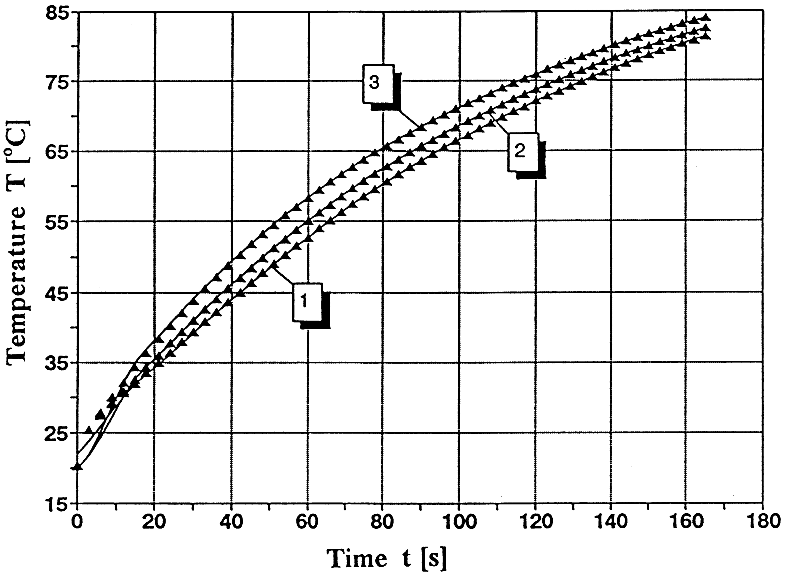

Fig. 12. Time temperature history at nodes 1–3 estimated from exact temperature measurements at nodes 9–15; ▲ 'exact temperature; —, inverse solution.

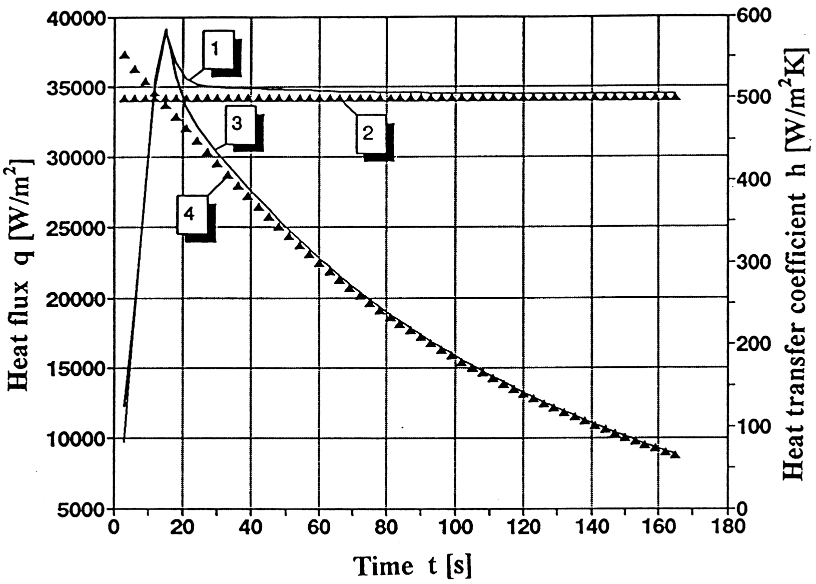

Fig. 13. Estimated surface heat flux and heat transfer coefficient at node 2 based on exact temperature measurements at nodes 9–15: 1, inverse solution for heat transfer coefficient; 2, exact value of heat transfer coefficient; 3, inverse solution for surface heat flux; 4, exact value of surface heat flux.

by hot water. The water temperature T_∞ changes with time as the hot water does not flow through the cylinder. The temperature distribution in the tube wall was calculated based on the measured outside surface temperature (Fig. 16). For the relatively narrow range of temperature changes, the mean thermal diffusivity is $\alpha = 1.2 \cdot 10^{-5}$ m^2 s^{-1} and thermal conductivity is $k = 44$ W m^{-1} K^{-1}. The temperature at the outside surface was

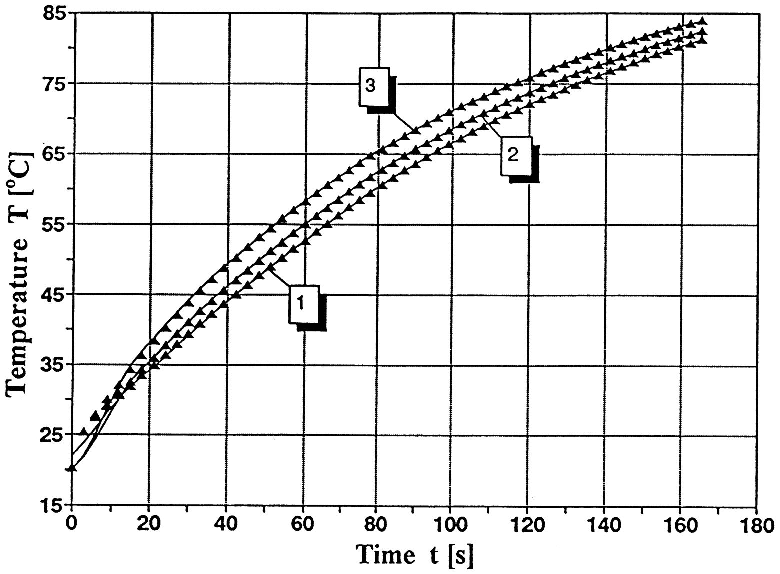

Fig. 14. Time temperature history at nodes 1–3 estimated from noisy temperature measurements at nodes 9–15: ▲, 'exact' temperature; —, inverse solution.

recorded at a rate of one reading per 5 s using a data acquisition system. The inverse analysis was performed at an on-line mode. The results are shown in Figs 16 and 17. To test the accuracy of the presented method, the temperature at the inside surface of the cylinder was also measured (Fig. 16).

The results show good accuracy despite the relatively small time step Δt. However, the accuracy for small time is not as good as for large time. This deviation is attributed to the small number of control volumes. The cylinder wall should be divided into more control volumes to achieve higher accuracy for smaller values of time. Finer division of the space domain into control volumes results in the higher order derivatives in the inverse solution and in its better accuracy. The temperature measurement errors must also be accounted for. The exact measurement of temperature at the surface of a solid subjected to cooling or heating by a fluid is extremely difficult.

Figure 17 shows the estimated surface heat flux and heat transfer coefficient at the inside surface of the cylinder. During early time transients, $h(t)$ increases to a maximum value. The calculated $q_s(t)$ and $h(t)$ functions have their maximum about 30 s after flooding the cylinder with hot water. Then the heat transfer coefficient decreases with time as the temperature difference between the heating fluid and the cylinder surface $\Delta T = T_\infty - T_s$ decreases. Sudden flooding of the cylinder produces the coupled flow and thermal fields along the vertical cylinder surface, which cause a high heat flux and heat transfer coefficient values.

5. Conclusions

The new space marching method for one- and multi-dimensional inverse heat conduction problems has been presented. The method described is mathematically simple and computationally efficient. To achieve high accuracy of the solution, in contrary to the direct problems, only a small number of control volumes can be considered. Another unique advantage of the present formulation is that it is noniterative and nonsequential. It is worth pointing out that the method requires no information about the initial temperature distribution. The inverse solution developed in the paper depends only on the initial temperature distribution in the direct region. Temperature distribution in the inverse region at $t = 0$ results from the solution of the inverse problem. The initial poor accuracy is a result of large distance of the temperature sensor from the exposed surface and the abrupt change of the fluid temperature which make the inverse method inaccurate. When the temperature sensor is placed far from the active (exposed) surface, as in our case, then the measured temperature is noticeably delayed and damped in comparison with time changes occurring at the active surface. Thus, it is impossible to determine exactly the initial condition in the inverse region in this case, because the calculated time derivatives of the measured temperature at $t = 0$ are of low accuracy. The initial temperature distribution in the body could be determined much more precisely, if the temperature sensor is placed near the active surface.

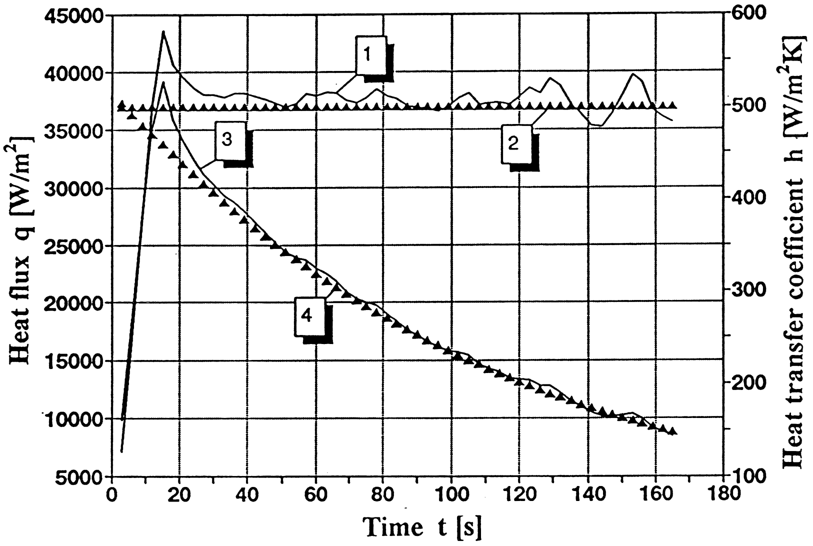

Fig. 15. Estimated surface heat flux and heat transfer coefficient at node 2 based on noisy ($\sigma = 0.05$) temperature measurements at nodes 9–15: 1, inverse solution for heat transfer coefficient; 2, exact value of heat transfer coefficient; 3, inverse solution for surface heat flux; 4, exact value of surface heat flux.

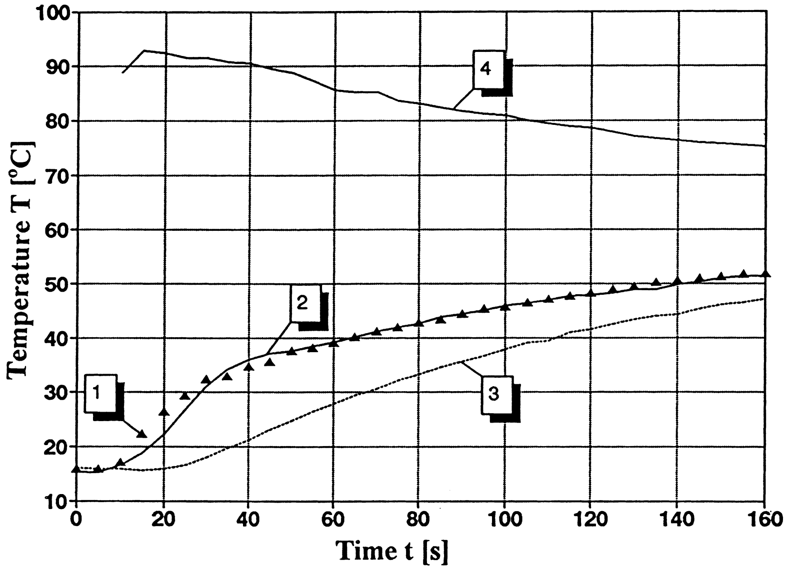

Fig. 16. Comparison of the measured surface temperature with inverse solution based on temperature measurements at outer surface: 1, measured temperature; 2, inverse solution; 3, temperature of the outer surface (input data); 4, fluid temperature.

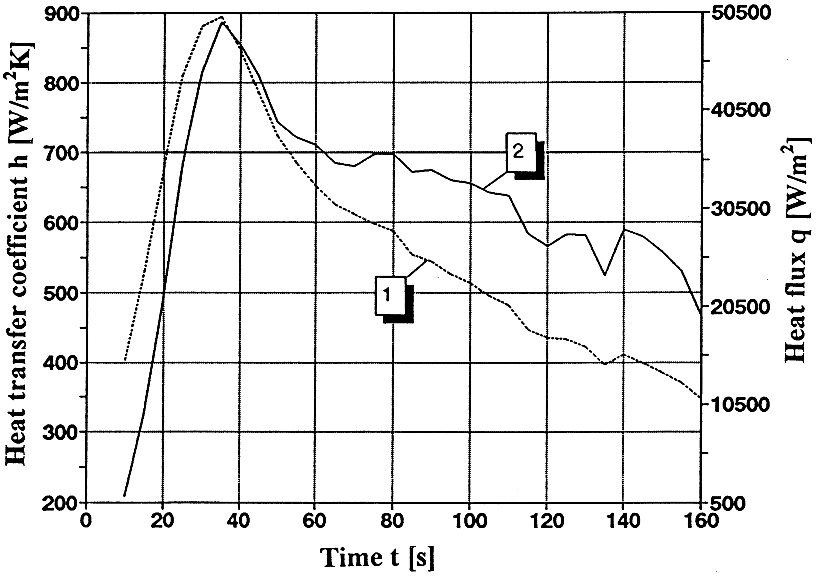

Fig. 17. Calculated heat flux and heat transfer coefficient at inner surface based on temperature measurements at outer surface: 1, heat flux; 2, heat transfer coefficient.

References

[1] J.V. Beck, B. Blackwell, Ch.R.St. Clair, Inverse heat conduction, Ill-posed Problems, Wiley-Interscience Publication, New York, 1985.

[2] A. Arakawa, R. Takahashi, Real time application of filtering theory to one-dimensional heat conduction, Nuclear Engineering and Design 70 (1982) 215–221.

[3] O.M. Alifanov, A.V. Nenarokomov, Boundary inverse heat conduction problem in external formulation, in: N. Zabaras, K.A. Woodbury, M. Raynaud (Eds.), Inverse Problems in Engineering: Theory and Practice, ASME, New York, 1993, pp. 31–38.

[4] E.P. Scott, J.V. Beck, Analysis of order of the sequential regularization solutions of inverse heat conduction problems, Transactions of the ASME, Journal of Heat Transfer 111 (1989) 218–214.

[5] G.P. Flach, M.N. Özişik, An adaptive inverse heat conduction method with automatic control, Transactions of the ASME, Journal of Heat Transfer 114 (1992) 5–13.

[6] Y.F. Hsu, B. Rubinsky, K. Mahin, An inverse finite element method for the analysis of stationary arc welding processes, Transactions of the ASME, Journal of Heat Transfer 108 (1986) 734–741.

[7] T.R. Hsu, N.S. Sun, G.G. Chen, Z.L. Gong, Finite element formulation for two-dimensional inverse heat conduction analysis, Transactions of the ASME, Journal of Heat Transfer 114 (1992) 553–557.

[8] H.J. Reinhardt, A numerical method for the solution of two-dimensional inverse heat conduction problems, International Journal for Numerical Methods in Engineering 32 (1991) 363–383.

[9] J. Taler, Nonlinear steady-state inverse heat conduction problem with space-variable boundary conditions, Transactions of the ASME, Journal of Heat Transfer 114 (1992) 1048–1051.

[10] J. Taler, Numerical solutions for general inverse heat conduction problem, Wärme- und Stoffübertragung 27 (1992) 505–513.

[11] A. Haji-Sheikh, F.P. Buckingham, Multidimensional inverse heat conduction using the Monte Carlo Method, Transactions of the ASME, Journal of Heat Transfer 115 (1993) 26–33.

[12] K.A. Woodbury, S.K. Thakur, A two-dimensional inverse heat conduction algorithm, in: N. Zabaras, K.A. Woodbury, M. Raynaud (Eds.), Inverse Problems in Engineering: Theory and Practice, ASME, New York, 1993, pp. 219–226.

[13] Ch.F. Weber, Analysis and solution of the ill-posed inverse heat conduction problem, Mass Transfer 24 (1981) 1783–1792.

[14] M. Raynaud, J. Bransier, A new finite difference method for nonlinear inverse heat conduction problem, Num. Heat Transfer 9 (1986) 27–42.

[15] E. Hensel, R.G. Hills, An initial value approach to the inverse heat conduction problem, Transactions of the ASME, Journal of Heat Transfer 108 (1986) 248–256.

[16] J.J. Serra, J.M. Gineste, S. Serror, Experimental investigation of heat transfer in a gun barrel based on a space marching inverse conduction method, in: N. Zabaras, K.A. Woodbury, M. Raynaud (Eds.), Inverse Problems in Engineering: Theory and Practice, ASME, New York, 1993, pp. 323–328.

[17] J. Taler, Semi-numerical method for identification of temperature fields from measurements at interior locations, Proceedings of the XV-th Polish Conference on Thermodynamics, Gliwice-Kokotek 2 (1993) 653–659 (in Polish).

[18] W. Zima, Prediction of transient temperature and heat

flux distributions at inside surface based on temperature measurements at outside solid surface, Measurements in Production Processes, Proceedings of the Fifth Polish Technical Conference, Cracow, 1994, pp. 277–283 (in Polish).

[19] J. Stefan, Über die Theorie der Eisbildung insbesondere über Eisbuldung im Polarmeere, S.-B. Wien. Akad. Mat. Natur. 98 (1889) 965–983.

[20] O.E. Burggraf, An exact solution of the inverse problem in heat conduction theory and applications, Transactions of the ASME, Journal of Heat Transfer 86 (1964) 373–382.

[21] B.R. Baliga, S.V. Patankar, Elliptic systems, finite-element method II, in: W.J. Minkowycz, E.M. Sparrow, G.E. Schneider, R.H. Pletcher (Eds.), Handbook of Numerical Heat Transfer, Wiley, New York, 1988.

[22] G.E. Schneider, Finite-element methods for conduction, in: G.F. Hewitt (Ed.), Handbook of Heat Exchanger Design, Begell House, New York, 1992.

[23] G.A. Korn, T.M. Korn, Mathematical Handbook, Chap. 20, McGraw-Hill, New York, 1968.

[24] C.F. Gerald, P.O. Wheatley, Applied Numerical Analysis, 5th ed., Addison-Wesley, Reading, MA, 1994, pp. 327–328.

[25] Subroutine NORNG—Normal Random Number Generator, FORTRAN: Scientific Subroutine Library, IBM, 1984.